

VISION-INSPIRED IMAGE QUALITY ASSESSMENT FOR RADAR-BASED HUMAN ACTIVITY REPRESENTATIONS

Huy Trinh, Davis Liu, Munia Humaira, Peter Lee, Zhou Wang

University of Waterloo

ABSTRACT

Radar-based human activity recognition has gained attention as a privacy-preserving alternative to vision and wearable sensors, especially in sensitive environments like long-term care facilities. Micro-Doppler spectrograms derived from FMCW radar signals are central to recognizing dynamic activities, but their effectiveness is limited by noise and clutter. In this work, we use a benchmark radar dataset to reimplement and assess three recent denoising and preprocessing techniques: adaptive preprocessing, adaptive thresholding, and entropy-based denoising. To illustrate the shortcomings of conventional metrics in low-SNR regimes, we evaluate performance using both perceptual image quality measures and standard error-based metrics. We additionally propose a novel framework for static activity recognition using range-angle feature maps to expand HAR beyond dynamic activities. We present two important contributions: a temporal tracking algorithm to enforce consistency and a no-reference quality scoring algorithm to assess RA-map fidelity. According to experimental findings, our suggested techniques enhance classification performance and interpretability for both dynamic and static activities, opening the door for more reliable radar-based HAR systems.

Index Terms— Radar, Spectrogram, Denoising, Micro-Doppler, Image Quality Assessment

1. INTRODUCTION

Radar technology possesses a longstanding history of application across various sectors, including aerospace, defence, and automotive systems. More recently, especially in settings where non-invasiveness and privacy are crucial, such as long-term care (LTC) facilities, it has surfaced as a promising tool for human activity recognition (HAR). Wearable devices and RGB cameras sometimes generate privacy and security issues despite their performance, but radar provides a contactless and privacy-preserving option. Noise in the raw radar signals from sources, including thermal noise, electrical interference, and environmental clutter, challenges the dependability of radar-based HAR. These elements can hide weak reflections and raise the background floor, therefore hindering precise activity detection. Moreover, many present studies de-

pend on low-resolution radar systems, which are susceptible to noise contamination when extracting signals [1], [2].

Extensive research has been done on various preprocessing and denoising methods that focus on dynamic and basic activity recognition tasks. Deep learning-driven techniques, such as inferencing and testing on machine learning models, are then used to assess how effective these algorithms are. However, their numerical impact, visual explainability of models, and method comparisons have not been thoroughly examined. Additionally, to the best of our knowledge, there aren't many studies on the recognition of static activities or slowly changing motions. The main contributions of our research can be summarized in two points:

- We quantitatively evaluate the efficiency of recent radar-spectrogram-based denoising and preprocessing methods using error-based metrics and image quality assessment.
- We propose algorithms for scoring quality and tracking Range-Angle (RA) feature maps for stationary activities.

2. DYNAMIC ACTIVITIES EVALUATION

Since radar spectrograms containing human activities are often very noisy, it is important to investigate multiple denoising approaches to obtain the optimum one for our use case. To achieve this, we replicated and reimplemented the three latest denoising and preprocessing methods in the radar-based HAR domain.

2.1. Adaptive Preprocessing

An adaptive resolution preprocessing (APr) technique has been suggested by Park et al. [3] to improve micro-Doppler (mD) spectrogram-based HAR using frequency-modulated continuous wave (FMCW) radar signals. Conventional spectrograms employ a fixed time-frequency resolution, which frequently falls short of capturing the characteristics of the entire range of motion, particularly for low-frequency or subtle movements. The authors address this by introducing a resolution-adaptive spectrogram, which uses the energy distribution of the mD signatures to non-linearly adjust frequency resolution. In particular, the technique locates each spectrogram's active frequency range and uses logarithmic mean-square scaling to improve resolution in lower-

frequency bands, which are usually where fine motion details show up. Compared to traditional representations, this adaptive method generates more discriminative spectrograms, which enhances the performance of the deep learning model.

2.2. Adaptive-Thresholding

An adaptive thresholding algorithm (ATh) proposed by Li et al.[4] offers a low-computation, high-accuracy solution for radar-based human activity recognition, making it well-suited for multi-domain mD signatures and resource-constrained systems. The method consists of three stages: signal pre-processing, adaptive thresholding, and classification. In pre-processing, a Hamming-windowed Fast Fourier Transform (FFT) generates a range-time map from time-domain radar pulses, followed by a 4th order Butterworth filter[5] to suppress noise. A Short-Time Fourier Transform (STFT), using a 0.2 second Hamming window with 95% overlap, produces the mD spectrogram. Adaptive thresholding converts the spectrogram to grayscale and iteratively updates a threshold based on average pixel intensity until convergence (typically at $V = 0.1$). The resulting binary mask is used to generate masked spectrograms and phase-related images. The final classification is performed using a support vector machine (SVM) algorithm.

2.3. Entropy-Based Denoising

The third reimplemented algorithm, proposed by Nguyen et al. [6], applies a two-step entropy-based denoising (EBD) approach for spectrogram enhancement and classification. The first step identifies the optimal range-bin interval containing the most motion-relevant signal energy. This is achieved by computing the FFT of each range-bin across the slow-time axis, identifying the most frequently occurring peak location, and evaluating surrounding intervals via STFT. The interval with the lowest average Shannon entropy, H_{avg} , is selected as optimal.

$$r_{opt} = \arg \min_{1 \leq q \leq Q} H_{avg}(range_{r_q}) \quad (1)$$

In the second step, adaptive spectrogram thresholding is applied within the selected interval. A Gaussian-windowed STFT is computed frame-by-frame, and a dynamic cut-threshold is generated based on local average energy. This masking function reduces background noise while preserving key micro-Doppler signatures, ultimately improving the clarity of the spectrogram for downstream classification tasks.

2.4. Experiment Setup

After implementing the algorithms discussed above, we evaluated their performance using the dataset provided in [6]. The raw signal dataset comprises 19,800 samples, generated by combining 11 distinct activities, 5 aspect angles,

and 60 iterations. The first step in our processing pipeline involves generating spectrograms for each radar signal file. Following this, white Gaussian noise (WGN) is added at 5 different signal-to-noise ratio (SNR) levels: -10 dB, -5 dB, 0 dB, and 10 dB. The resulting spectrograms are illustrated in Figure 1. These noisy spectrograms are then processed using three reimplemented denoising methods, as well as our combined APr and ATh method (APr+ATh). The Structural

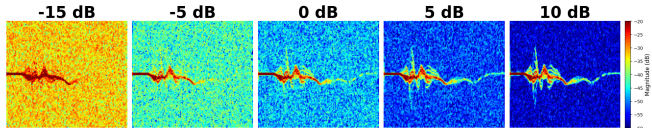


Fig. 1: Spectrogram after adding 5 different White Gaussian noise levels.

Similarity Index Measure (SSIM) [7], a perceptual metric that evaluates image quality based on structural fidelity, is used to evaluate the denoised spectrogram outputs, which have been done quite rarely before [8]. The similarity between image structure and contrast is the main focus of SSIM. We used several common quantitative evaluation metrics, such as Mean Squared Error (MSE), Mean Absolute Error (MAE), Root Mean Squared Error (RMSE), Peak Signal-to-Noise Ratio (PSNR), and the Pearson Correlation Coefficient.

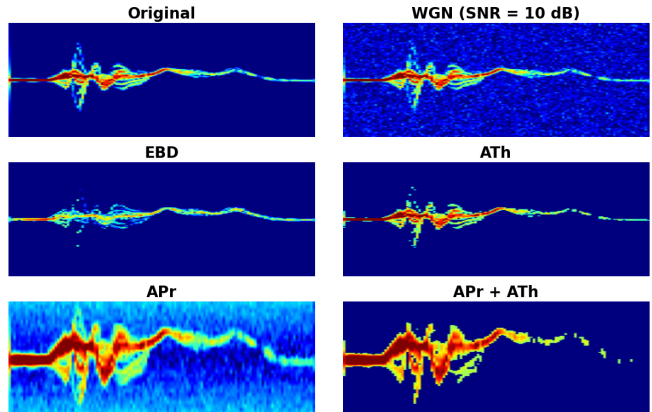


Fig. 2: Spectrogram results for Walking (W): original spectrogram (top-left), noisy spectrogram (top-right) and 4 methods under WGN (SNR = 10 dB).

Figure 2 shows the result of 4 methods along with the original noise-free and noisy spectrograms. Its corresponding evaluation metrics are shown in Table 1. It can be inferred from the table that the ATh algorithm removes noise selectively and preserves most of the detail in case SNR = 5 dB. EBD algorithm, however, preserves large-scale intensity distribution with high correlation but degrades to local structures. The APr algorithm effectively adjusted the frequency resolution, enabling mD signatures to span a broader

frequency range. This ensures optimal representation by dynamically expanding the active frequency, though it also has the unintended effect of scaling noise within the calculated range. Applying ATh after APr removes these noises for a cleaner representation but can also remove fine main signal details in this case.

Table 1: Evaluation metrics result for walking (W) under White Gaussian Noise (SNR = 10 dB).

METRICS	NS	EBD	ATh	APr	APr + ATh
MSE	5053.2	12953.8	4785.7	6254.1	5043.3
MAE	63.82	107.48	62.15	73.05	65.58
RMSE	71.08	113.9	69.17	79.08	71.01
PSNR (dB)	-19.69	-23.78	-19.46	-20.62	-19.68
Pearson Corr	0.572	0.6168	0.6006	0.4462	0.5561
SSIM	0.365	0.3639	0.4109	0.2881	0.3227

Bold indicates the best (optimal) value in each row

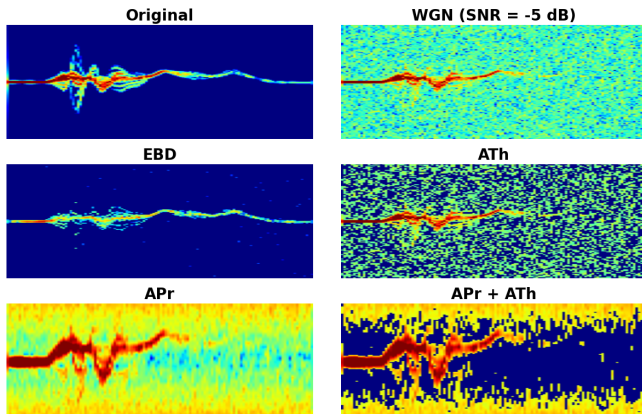


Fig. 3: Spectrogram results for Walking (W): original spectrogram (top-left), noisy spectrogram (top-right) and 4 methods under WGN (SNR = -5 dB).

Table 2: Evaluation metrics result for walking (W) under White Gaussian Noise (SNR = -5 dB).

METRICS	NS	EBD	ATh	APr	APr + ATh
MSE	7184.1	13501.9	6152.6	8365.6	6935.6
MAE	77.81	110.18	71.01	84.86	75.32
RMSE	84.76	116.19	78.43	91.46	83.28
PSNR (dB)	-21.22	-23.96	-20.55	-21.8864	-21.07
Pearson Corr	0.329	0.533	0.225	0.073	-0.058
SSIM	0.261	0.305	0.175	0.227	0.177

Bold indicates the best (optimal) value in each row

Under severe noisy (-5 dB) condition (Figure 3, Table 2), EBD shows a better ability to denoise although there are some speckles left in the background, which may explain lower metrics compared to its corresponding values in Table 1. ATh is quite prone to very high noise levels, whose SNRs are negative. However, its pixel error (MSE, RMSE, PSNR) metrics

are lower than those of EBD. SSIM, on the other hand, shows a more reasonable alignment in both cases. Thus, SSIM can be used as a cost function when training deep learning models for fidelity-based applications such as Generative Adversarial Network (GAN)-based [9] reconstruction or synthetic spectrogram generators.

According to our study, depending only on error-based metrics can be deceptive, especially when there is a low SNR as perceptual fidelity rather than pixel-level similarity is needed to preserve subtle mD signatures, which are essential for precise human activity recognition. Moreover, we find that the SSIM metric does not always match the results of the APr preprocessing method, indicating that structural similarity might not adequately convey the perceptual quality enhancements brought about by adaptive range-bin selection. This motivates a need for better tailored metrics to specifically evaluate the quality of spectrograms and also align better with the model’s perception when training a deep-learning-based denoiser. A good spectrogram quality metric should take into consideration important characteristics like background noise suppression and the clarity and continuity of ridge patterns that represent mD signatures.

3. PROPOSED PRE-PROCESSING METHODS FOR STATIC ACTIVITIES’ FEATURE MAPS

The aforementioned techniques and assessments have concentrated on dynamic human activities that are distinguished by unique mD signatures; however, many real-world situations, particularly in settings like LTC facilities, also call for accurate identification of static or slowly changing activities (e.g., sitting, standing, watching television, transitioning from sitting to standing, etc.). The complete range of human behaviours that are present in these kinds of environments cannot be captured by dynamic activity recognition alone. Due to the lack of research in this field, it is especially intriguing. Static or slow-moving activities generate minimal Doppler shifts, rendering conventional mD spectrograms ineffective. As a result, the Doppler-time frequency spectrogram in section 2 is not suitable for stationary objects, as it shows horizontal lines in the Doppler-time spectrogram, which is indistinguishable from static clutter and background noise. FMCW radar retains the ability to localize static reflectors through beat-frequency processing and spatial filtering. By analyzing the phase difference between transmitted and received chirps, FMCW systems extract high-resolution range profiles and, when combined with adaptive beamforming, we can obtain RA maps that can discriminate stationary objects in space [10]. Ali et al. [11] leverage this capability by computing Capon RA maps and extracting spatial features to train machine learning classifiers for static pose recognition[12].

To assess the suitability of existing RA-map preprocessing for static activity recognition, we first reimplemented their pipeline comprising range-FFT, range-Doppler spectrogram



Fig. 4: Our measurement setup in the long-term care facility (left) and our laboratory (right).

generation, and Capon beamforming and applied it to our collected dataset. For this study, we collected a dedicated dataset of static activities in two different environments (our laboratory as dataset 1 and long-term care facility as dataset 2) using an off-the-shelf 60 GHz radar *BGT60TR13C* radar from Infineon, with one transmitter and three receivers [13]. Dataset 2 captures a range of basic postures: lying on floor (A0), lying on sofa (A1), sitting on floor (A2), sitting on sofa (A3), standing (A4), slow walking (A5) and minimal movements: getting up from sofa (A6), picking objects from floor (A7), and picking up objects from a table (A8) while dataset 1 was used for validation. The experimental setups are shown in the figure 4. The resulting RA feature maps exhibit wide variability in spatial fidelity, as shown in figure 6. To quantify how these map-quality variations impact learning, we trained a lightweight 3D Convolution Neural Network (CNN) on the RA maps from dataset 2. The model consists of three 3D convolutional blocks (kernel size of 3, channel depths of 32, 64, 128), each followed by batch normalization, ReLU activation, max-pooling and dropout, and 3 fully connected layers. We used Grad-CAM [14] to visualize the network’s class-discriminative attention on individual frames. Figure 5 shows Grad-CAM overlays for frame 5 of class lying on floor (class 0 - top row) and class sitting on floor (class 2 - bottom row): the red box denotes the ground-truth target blob, and the green box highlights the region to which the model attends. In the top row, the model incorrectly focuses on a background lump, whereas in the bottom example, its attention aligns well with the annotated target. These failure modes demonstrate that the CNN model can learn spurious clutter features when RA-map quality is poor, leading to brittle static-activity classification. Motivated by these observations, we propose no-reference Range-Angle feature-map ‘Quality Scoring and ‘Temporal Tracking’ algorithms.

3.1. Quality Scoring Algorithm

To quantify the fidelity of the RA-map without requiring a clean reference, we introduce a “lumps+subpeak” algorithm that produces a frame-level *cleanliness score* $S \in [0, 1]$ by combining three feature-map characteristics: (i) energy concentration in high-intensity blobs, (ii) purity of each blob via

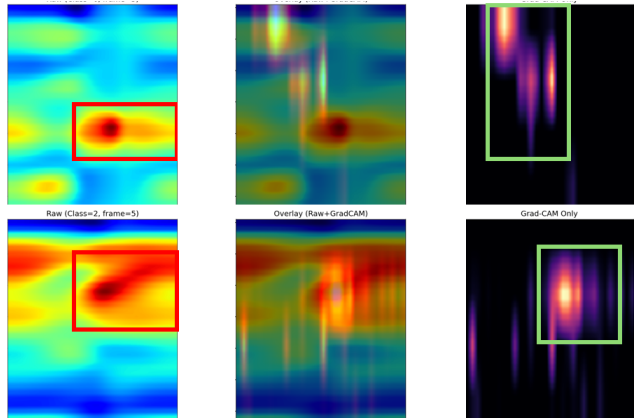


Fig. 5: Grad-CAM visualization on Range–Azimuth feature maps for frame 5 of static activities. Top row: class A0 (lying on floor); bottom row: class A2 (sitting on sofa). In each row, the left panel shows the raw RA map with the red box indicating the ground-truth target region, the center panel overlays the Grad-CAM heatmap (magma colormap), and the right panel highlights the network’s attended region (green box).

sub-peaks, and (iii) global peak prominence.

High-intensity lump is often but not necessarily true scatterer, while multiple scatters and subpeaks will result in penalty. These will capture cases of bad-quality feature maps that contain different lumps or a true lump that is a burden in the background. By empirical study, the hyperparameters were set to a percentile threshold of $pct = 90$, a subpeak penalty $\alpha = 3$ for single peak (and $\alpha = 0.1$ when multiple peaks are present), and fusion weight $w_1 = 0.25$ and $w_2 = 0.75$. These values were tuned according to dataset 2 and then validated on dataset 1, demonstrating that the cleanliness scorer generalizes robustly across two very different environments. The resulting scores obtained from algorithm 1 for representative RA maps are shown in Figure 6.

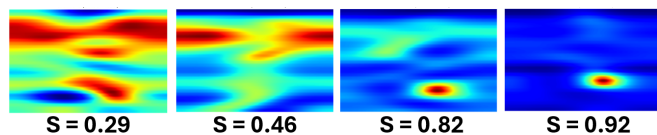


Fig. 6: Scores calculated from our proposed algorithm corresponding to features map.

3.2. Temporal Tracking Algorithm

To enforce temporal consistency and generate reliable region proposals, we implement a lump-tracking algorithm that links the primary scatterer across all frames. At each frame t , we first detect all high-intensity lumps and compute their cleanliness scores S_t via Algorithm 1. If the feature map’s score satisfies $S_t \geq \tau$ threshold (we use $\tau = 0.8$), we accept it imme-

Algorithm 1 Calculate frame score based on Lump + Peak Scores

```

1:  $lumps \leftarrow \text{LUMPSFROMFRAME}(X, pct)$  {find connected blobs above percentile}
   {detect sub-peak inside lumps}
2:  $subpeakCount \leftarrow 0$ 
3:  $maxVal \leftarrow \max(subArray)$ 
4:  $absThresh \leftarrow \gamma \times maxVal$ 
5: for all lump  $L$  in  $validLumps$  do
6:    $coords \leftarrow \text{PEAKLOCALMAX}(subArray, d_{min}, absThresh)$ 4.

7:    $subpeakCount \leftarrow subpeakCount + |coords|$ 
8: end for
9:  $lumpsPenalty \leftarrow \alpha \times (subpeakCount - 1)$ 
10:  $leftoverRatio \leftarrow \frac{E_{total} - E_{main}}{E_{main}}$ 
11:  $lumpsScore \leftarrow \frac{1}{1 + leftoverRatio + lumpsPenalty}$ 
12:  $lumpsScore \leftarrow \max(0, \min(lumpsScore, 1))$ 
13:  $p \leftarrow \max(X)$  {global peak}
14:  $\mu \leftarrow \text{mean}(X)$ 
15:  $\sigma \leftarrow \text{std}(X) + 10^{-9}$ 
16:  $peakness \leftarrow \max\{0, (p - \mu)/\sigma\}$ 
17:  $peakScore \leftarrow 1 - \exp(-\phi \times peakness)$ 
18:  $peakScore \leftarrow \max(0, \min(peakScore, 1))$ 
19:  $w1 \leftarrow 0.2, w2 \leftarrow 0.8$  {weights}
20:  $S \leftarrow (lumpsScore)^{w1} + (peakScore)^{w2}$ 
21:  $S \leftarrow \max(0, \min(S, 1))$ 
22: return  $S$ 

```

diately as the tracked target. Otherwise, we perform nearest-centroid gating: we compare the previous frame’s centroid c_{t-1} to each candidate lump c_i and select the one with maximum energy within a distance threshold d (in our case $d = 30$). We maintain this matching over a sliding window of five frames that corresponds to 0.5 seconds data for smooth transient dropouts. In Figure 7, the chosen lump is outlined in red, while all other detected lumps are shown in blue.

Once the target blob is identified, we generate 2 complementary masks for downstream processing (Figure 8): soft and hard masks. For the soft mask, weights radially decay from the tracked centroid to the whole maps, while weights are binary region of interest (ROI) (strictly 1 within the bounding region and 0 outside). These masks are then applied multiplicatively to each RA map, biasing the CNN’s attention toward the temporally consistent scatterer and suppressing background clutter. Together, our no-reference quality scorer and temporal tracker will provide both precise region annotations for training and robust spatial priors at inferencing. This combination helps improve robustness and interpretability in radar-based static activity recognition.

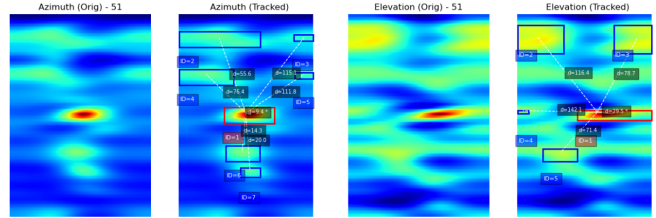


Fig. 7: Range-Azimuth and Range-Elevation feature maps of frame 51 (class 2) and their tracking results (columns 2 and

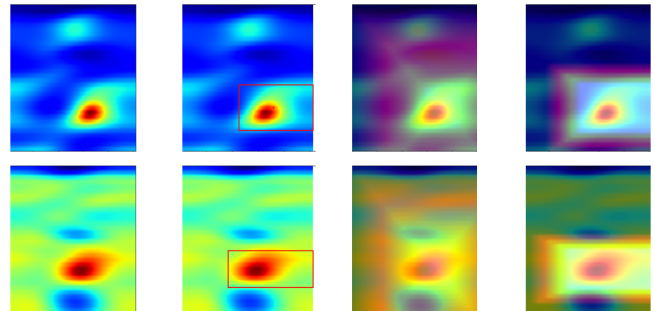


Fig. 8: Example of Range-Azimuth maps and their computed masks. Columns 1-2: Raw RA maps and detected bounding box overlay. Column 3: Soft masks. Column 4: Hard masks.

4. CONCLUSION

Our project investigated radar-based HAR in both dynamic and static activity regimes. We used three recent preprocessing and denoising techniques for dynamic activities and evaluated them using both perceptual image quality metric SSIM and conventional error-based metrics, e.g., MSE, PSNR, etc. The findings demonstrate the shortcomings of traditional metrics in noisy settings and emphasize the necessity of perceptually aligned metrics for deep learning-based denoiser training. Our novelty features a radar spectrogram processing pipeline based on range-angle feature maps to tackle the frequently disregarded problem of static activity recognition. Among our contributions are a temporal tracking algorithm for consistency across frames and a no-reference “lumps+subpeak” quality scoring algorithm for measuring RA-map fidelity. By using these techniques, clutter is reduced and the model’s focus is directed toward significant spatial features.

Our study suggests, radar-based HAR systems’ resilience is greatly increased when adaptive signal processing and customized spatial analysis are combined. Future research will integrate our tracking-and-masking framework into end-to-end deep learning pipelines for continuous activity monitoring in real-world scenarios and investigate joint time-frequency-spatial resolution adaptation.

5. REFERENCES

- [1] Hajar Abedi, Ahmad Ansariyan, and George Shaker, "Contactless in-bed detection using a low-cost low-resolution radar," in *2024 IEEE SENSORS*, 2024, pp. 1–4.
- [2] Joshua Visser, Hajar Abedi, Sachin Karmani, and George Shaker, "Ai based activity monitoring in washrooms using low-resolution radar," in *2025 IEEE MTT-S Latin America Microwave Conference (LAMC)*, 2025, pp. 78–81.
- [3] Do-Hyun Park, Min-Wook Jeon, and Hyoung-Nam Kim, "Resolution-adaptive micro-doppler spectrogram for human activity recognition," *arXiv preprint arXiv:2411.15057*, 2024.
- [4] Zhenghui Li, Julien Le Kernec, Qammer Hussain Abbasi, Francesco Fioranelli, Shufan Yang, and Olivier Romain, "Radar-based human activity recognition with adaptive thresholding towards resource constrained platforms," *Scientific Reports*, vol. 13, 2023.
- [5] S. Butterworth, "On the Theory of Filter Amplifiers," *Experimental Wireless & the Wireless Engineer*, vol. 7, pp. 536–541, Oct. 1930.
- [6] NgocBinh Nguyen, MinhNghia Pham, Van-Sang Doan, and VanNhu Le, "Improving human activity classification based on micro-doppler signatures of fmcw radar with the effect of noise," *PLOS ONE*, vol. 19, no. 8, pp. 1–26, 08 2024.
- [7] Zhou Wang, A.C. Bovik, H.R. Sheikh, and E.P. Simoncelli, "Image quality assessment: from error visibility to structural similarity," *IEEE Transactions on Image Processing*, vol. 13, no. 4, pp. 600–612, 2004.
- [8] Yuan He, Xinyu Li, Runlong Li, Jianping Wang, and Xiaojun Jing, "A deep-learning method for radar micro-doppler spectrogram restoration," *Sensors*, vol. 20, no. 17, 2020.
- [9] Ibrahim Alnujaim, Shobha Sundar Ram, Daegun Oh, and Youngwook Kim, "Synthesis of micro-doppler signatures of human activities from different aspect angles using generative adversarial networks," *IEEE Access*, vol. 9, pp. 46422–46429, 2021.
- [10] Infineon Team, "Detection of stationary objects using radar technology," *Infineon Community Knowledge Base*, January 2024, [Online]. Available: <https://community.infineon.com/t5/Knowledge-Base-Articles/Detection-of-stationary-objects-using-Radar-technology/ta-p/681036> [Accessed: April 15, 2025].
- [11] Ali Samimi Fard, Mohammadreza Mashhadigholamali, Samaneh Zolfaghari, Hajar Abedi, Mainak Chakraborty, Luigi Borzi, Masoud Daneshtalab, and George Shaker, "Exploring fmcw radars and feature maps for activity recognition: A benchmark study," *arXiv preprint arXiv:2503.05629*, 2025.
- [12] J. Capon, "High-resolution frequency-wavenumber spectrum analysis," *Proceedings of the IEEE*, vol. 57, no. 8, pp. 1408–1418, 1969.
- [13] Infineon Technologies AG, "Bgt60tr13c 60ghz radar sensor," *Infineon Product Page*, March 2024, [Online]. Available: <https://www.infineon.com/cms/en/product/sensor/radar-sensors/radar-sensors-for-iot/60ghz-radar/bgt60tr13c/> [Accessed: April 15, 2025].
- [14] Ramprasaath R. Selvaraju, Michael Cogswell, Abhishek Das, Ramakrishna Vedantam, Devi Parikh, and Dhruv Batra, "Grad-cam: Visual explanations from deep networks via gradient-based localization," *International Journal of Computer Vision*, vol. 128, no. 2, pp. 336–359, Oct. 2019.